PERGAMON

EFFECT OF VISCOUS GRAIN BRIDGING ON CYCLIC FATIGUE-CRACK GROWTH IN MONOLITHIC CERAMICS AT ELEVATED TEMPERATURES

J. M. McNANEY, C. J. GILBERT and R. O. RITCHIE†

Department of Materials Science and Mineral Engineering, University of California, Berkeley, CA 94720-1760, U.S.A.

Abstract—The bridging tractions developed behind a crack tip are considered for a stationary crack under cyclic loading conditions at elevated temperatures in high-toughness, monolithic ceramics. Assuming a temperature range where the grain-boundary phases are sufficiently soft such that bridging can occur due to a viscous layer in the boundary, a viscoelastic model is developed in which bridging forces associated with the shear resistance of the grain-boundary phase are transmitted across the surfaces of a crack. Throughout the work, cyclic and static damage mechanisms which may be operating ahead of the crack tip (e.g. creep cavitation) are ignored in order to focus exclusively on the role of viscous grain bridging. A primary goal is to incorporate microstructural details like grain shape, grain-boundary thickness, and glass viscosity, as well as the effects of external variables such as loading rate and temperature. A fully self-consistent numerical approach is adopted, which does not require any prescribed assumptions as to the shape of the crack-opening profile. The self-consistent solution is compared to an analytical solution for a simplified parabolic approximation of the crack-flank opening displacements. The model is applicable to a wide range of ceramic materials at elevated temperatures, and rationalizes the frequency and temperature sensitivity not generally observed in ceramics at room temperature. Solutions identify a non-dimensional group associated with microstructure and external loading conditions, and solutions are presented over a range of this parameter. © 1999 Acta Metallurgica Inc. Published by Elsevier Science Ltd. All rights reserved.

Keywords: Ceramics, structural; Mechanical properties, fatigue, high temperature; Crack bridging

1. INTRODUCTION

Elevated-temperature cyclic fatigue behavior in monolithic ceramics is poorly understood. Data are sparse, published observations are contradictory, and mechanistic understanding is lacking. This is due in part to the experimental complexity and expense involved in gathering necessary data. In fact, only recently have experimental techniques appeared which allow for consistent crack-growth monitoring in these materials at high temperatures, and even these methods are somewhat limited. The primary objective of the present work is to propose a micromechanical model to rationalize at least some of the existing observations. The work focuses on high toughness, liquid-phase sintered ceramics which contain amorphous grain-boundary films.

It is clear that in many monolithic ceramics, such as Al_2O_3, Si_3N_4, and SiC, the presence of secondary amorphous phases (with attendant low melting temperatures) dominates high-temperature mechanical properties. These films arise from liquid-phase sintering techniques in which reaction products between sintering additives and starting powders

segregate to grain boundaries and triple junctions [1]. Even in small quantities, e.g. as ∼1 nm thick continuous films, they can profoundly influence mechanical properties such as strength, toughness, creep, and subcritical crack growth [1–10].

Under quasi-static loading, subcritical crack growth at high homologous temperatures is reasonably well studied in ceramic materials. Stable crack-extension results from the growth and linkage of cavities along grain-boundary interfaces due to viscous flow of the secondary phase [2, 4, 6–8]. Under cyclic loading, however, very few data have been reported. At present, most of the high-temperature data have been generated in the form of stress-life (S/N) data on unnotched specimens in a very narrow range of ceramics [11–18]. Such data are difficult to interpret mechanistically since total life may include contributions from both the initiation and propagation of flaws. In addition, large amounts of scatter are inevitable due to the large sensitivity of life to initial flaw populations.

More recently, a few researchers have generated high-temperature cyclic crack-growth rate data in Al_2O_3, Si_3N_4, and several ceramic-matrix composites [10, 19–30]. Not only are such data

† To whom all correspondence should be addressed.

sparse, but there is essentially no consensus on either the mechanisms of crack growth or the relationship between cyclic and static crack-growth rates at high temperature. For example, two separate studies on hot-pressed Al_2O_3 and three separate studies on hot-pressed Si_3N_4 concluded that cyclic crack-growth rates are faster [10, 19], slower [22, 25], or the same [27–30] as corresponding growth rates under static loading at equivalent stress-intensity levels. In addition, experiments to determine the role of microstructure are limited [10, 25, 31].

Such experimental discrepancies are likely to be the result of the mutual competition between four distinct microstructural phenomena localized to the regions either ahead of or behind the crack tip, termed intrinsic or extrinsic, respectively: (i) intrinsic creep damage via cavitation and sliding of the grain-boundary amorphous films, (ii) intrinsic fatigue damage [which does not appear to exist at room temperature (e.g. Refs [32, 33])], (iii) extrinsic crack-tip shielding from the interlocking of bridging grains, and (iv) extrinsic crack-tip shielding from viscous grain-boundary films (or in some cases, entire viscous ligaments [34]) spanning the crack faces (Fig. 1). The nature of the grain-boundary films clearly plays a large role in determining the relative potency of each of these mechanisms, and can act to enhance growth rates by accelerating microstructural damage via promotion of creep cavitation and grain-boundary sliding [2, 6, 7], or reduce growth rates by promoting crack-tip shielding via viscous bridging [11, 34]. It is therefore likely that any microstructural parameter (such as grain size, grain-boundary thickness and impurity content) or external parameter (such as temperature and frequency) which alters the deformation beha-

vior of the grain boundary glass will have an effect on cyclic fatigue behavior.

In fact, recent observations on Al_2O_3 under cyclic loading which show reduced crack-growth rates [25], or in the case of S/N measurements increased time to failure [11, 17], have been attributed to the highly rate-dependent nature of viscous phase deformation [11, 34]. The cyclic growth rates measured in these cases are even lower than those predicted based on the assumption that cyclic crack extension is simply the accumulation of static creep damage [35]. It has been proposed that this measured reduction in growth rates is due to enhanced viscous bridging during load cycling; in these cases, glassy ligaments are indeed observed to span the crack faces [11, 34] (e.g. Fig. 2). Because the load-bearing capacity of a viscous bridge is directly proportional to strain or displacement rate, cyclic loading enhances crack-tip shielding and subsequently reduces crack-growth rates (all else being equal). Consistent with such a mechanism, experiments on Al_2O_3 and an Al_2O_3–SiC_w composite indicate that growth rates slow with increased test frequency (due to higher strain rates) and increase with temperature (due to reduced viscosity) [19, 24]. Similar trends are observed in Si_3N_4 [10, 27–29].

On the other hand, in the cases where cyclic crack-growth rates are actually faster than static rates, it is presumed that viscous bridging is inactive. In order to explain such behavior, grain-bridging degradation models similar to those invoked at room temperature [36, 37] have been proposed [10]. Indeed, there is evidence that in cases where viscous bridging is inactive, due to relatively low temperatures, frequencies or differing grain-boundary chemistry, the room-temperature bridging degradation models may be applicable to some materials even at
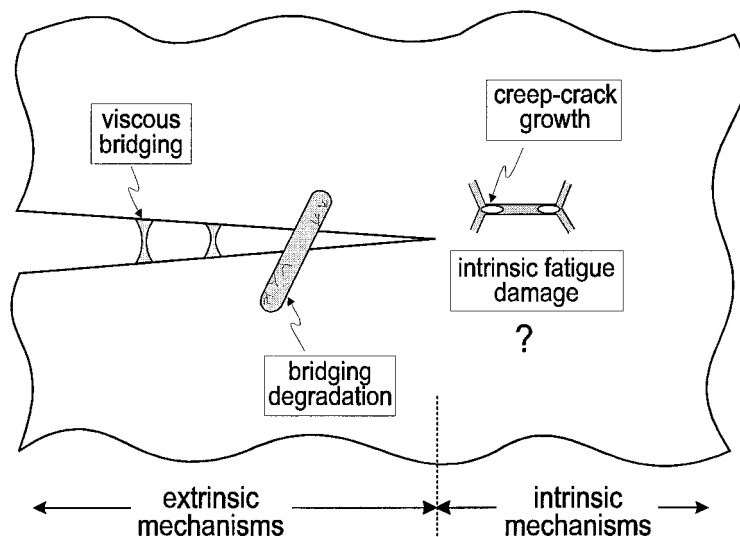

Fig. 1. Schematic illustration of the intrinsic (damage) and extrinsic (crack-tip shielding) mechanisms associated with elevated-temperature fatigue-crack growth in ceramics. Note that all mechanisms involve the grain-boundary phase.
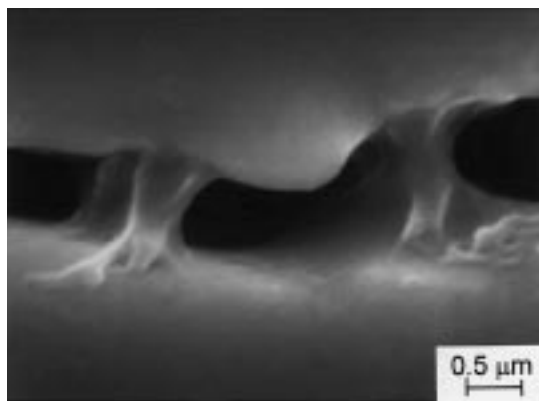
Fig. 2. Example of viscous ligament bridging during cyclic fatigue-crack growth in an *in situ* toughened SiC at 1200°C in an air atmosphere.
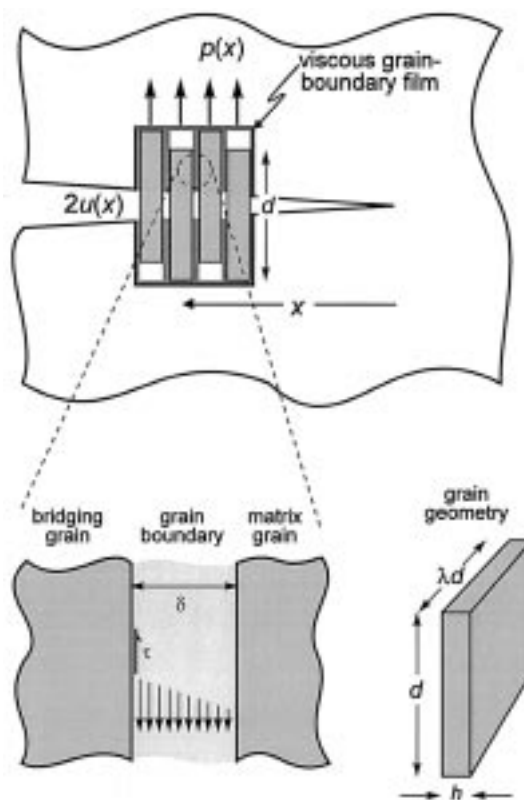

Fig. 3. Schematic illustration of the model for viscous grain-boundary film bridging at elevated temperatures, showing the development of the viscous force resulting from the velocity gradient in the film.

higher temperatures [10]. At present, however, experimental data are insufficient and sufficiently contradictory to make any unified model of this behavior unlikely.

The aim of the present work is to examine in detail the mechanics of the extrinsic viscous-film bridging process, with specific emphasis on its role in influencing elevated-temperature cyclic fatigue-crack propagation in ceramics. A model is developed which incorporates microstructural parameters such as grain size, and viscosity and thickness of the grain-boundary film, as well as external variables such as loading frequency, cyclic load amplitude, and load ratio (ratio of the minimum to maximum load). Unlike previous high-temperature viscous bridging models [11, 34], a fully self-consistent numerical approach is adopted. No limiting assumptions as to the shape of the crack-opening profile are made. Moreover, the model is not based on a viscous fluid film filling the crack (viscous-ligament bridging) [38], but rather bridging loads are transmitted across the crack walls due to the shear resistance of a grain-boundary film deforming between the matrix and the active bridging grain, allowing us to incorporate more microstructural detail. Our solutions identify a non-dimensional grouping associated with microstructure and external loading conditions, and solutions are presented over a range of this parameter. The model is applicable to a wide range of ceramic materials at elevated temperatures, and it rationalizes the frequency and temperature sensitivity not generally observed in ceramics at room temperature. Efforts are made to rationalize published observations on elevated-temperature ceramic fatigue using the model; the limitations of this approach are discussed.

2. VISCOUS GRAIN-BRIDGING MODEL

2.1. Bridging stress distribution

Calculations are performed using the microstructural model illustrated in Fig. 3. By assuming a temperature range where grain-boundary phases are sufficiently soft for viscous bridging to dominate, we develop a model in which bridging forces are transmitted across the crack flanks via shear resistance of the grain-boundary phase. The general strategy is to calculate local crack-tip stress fields based on an applied far-field loading cycle, and to use the magnitude of these local fields to rationalize macroscopically observed cyclic fatigue behavior. We ignore intrinsic cyclic and static damage mechanisms which may operate ahead of the crack tip (e.g. creep cavitation) in order to focus exclusively on the role of viscous grain bridging. Note, however, that the calculation of the near-tip driving force based on the actions of a bridging zone are crucial to understanding the severity of these intrinsic damage mechanisms.

As indicated in Fig. 3, the fundamental bridging element consists of a single grain located at distance, x, behind the crack tip. This grain is pulling out of its socket against the resistance of a visco-elastic grain-boundary phase of thickness, δ, which lies between it and the stationary matrix. An area fraction, A_f, of active bridging grains participates in the shielding process. For simplicity, the bridging grains are oriented perpendicular to the crack plane, and modeled as rectangular plates with

height, d, width, λd, and thickness, h [Fig. 3(a)]. Note that a physically meaningful geometry restricts the range of λ to between h/d, for a rod-like grain, to 1 for a plate-like grain. The matrix is considered stationary with the grain moving downward at a velocity, $v(x)$, where pullout occurs on only one side of the crack plane.

In order to develop the model the viscous response of the grain-boundary phase is first considered. Subsequent development of the elastic portion of the element's response is made by comparison of the elastic stress with the time-dependent viscous-induced stress.

The resulting shear stress, τ, acting along the side surface of a grain at position x [Fig. 3(b)] at the grain/grain-boundary interface is given by [39]

$$\tau = \eta \frac{v(x)}{\delta} \tag{1}$$

where η is the viscosity of the grain-boundary phase and $v(x)/\delta$ the velocity gradient in the glassy phase across the grain boundary, assuming a linear, steady-state velocity profile. The net bridging force in the grain acting normal to the crack walls is found by multiplying the shear stress, τ, by the area of the side-face of the grain which contacts the matrix. This area changes with total crack opening, $2u(x)$, and so the net force on the grain is given by $\tau[d - 2u(x)](h + \lambda d)$. For a force evenly distributed across the grain, the bridging stress, $p(x)$, is obtained by dividing this force by the cross-sectional area of the grain, λdh, and inserting the expression for τ given in equation (1):

$$p(x) = \frac{A_f \eta v(x)}{\delta h}[d - 2u(x)]\left(1 + \frac{h}{\lambda d}\right) \tag{2}$$

where the pre-factor A_f allows for partial coverage with bridging elements. The pullout velocity, $v(x)$, is given by the simple expression

$$v(x) = 2du(x)/dt = 2\dot{u}(x) \tag{3}$$

which yields the following $p(x)$ for an arbitrary $u(x)$:

$$p(x) = \frac{2\eta A_f}{\delta h}\dot{u}(x)[d - 2u(x)]\left(1 + \frac{h}{\lambda d}\right). \tag{4}$$

The shielding term resulting from viscous bridging, $K_b(t)$, is determined by integrating the bridging stress distribution over a bridging zone of length l_b. We use here the semi-infinite near-tip solution for $K_b(t)$, ignoring specimen geometry considerations and preserving the most generality [40]:

$$K_b = \left(\frac{2}{\pi}\right)^{1/2} \int_0^{l_b} \frac{p(x)}{\sqrt{x}} dx. \tag{5}$$

It should be noted, however, that any suitable geometry-dependent formulation for $K_b(t)$ may be employed by using an appropriate Green's function. Finally, the stress intensity experienced at the crack

tip is given by a superposition of the applied far-field loading, $K_a(t)$, and the shielding term resulting from viscous bridging, $K_b(t)$:

$$K_{tip}(t) = K_a(t) - K_b(t). \tag{6}$$

The primary computational difficulty is determining the crack-opening profile, $u(x)$, the bridging stress distribution, $p(x)$, and the bridging stress intensity, $K_b(t)$, in a fully consistent fashion. We initially simplify the task by making the common assumption of a parabolic crack-opening displacement profile controlled by the crack-tip stress intensity, K_{tip}. This assumption is frequently made, and we later compare the results with a self-consistent solution where no pre-conditions are placed on the form of $u(x)$.

2.2. Parabolic crack-opening profile formulation

For simplicity we treat the response of the grain-boundary phase as only viscous and assume a parabolic profile for $u(x)$ controlled by K_{tip}, as given by the near-tip traction-free, linear-elastic solution [41]:

$$u(x) = \frac{K_{tip}}{E_*}\left(\frac{8x}{\pi}\right)^{1/2} \tag{7}$$

where $E_* = E$ (Young's modulus) in plane stress and $E/(1 - v)^2$ in plane strain (v = Poisson's ratio). This parabolic profile is an often-used approximation (e.g. Refs [11, 34]) and has the advantage of being relatively easy to solve. Combining equations (4)–(7) yields the following non-linear differential equation:

$$K_{tip}(t) = K_a(t) - \beta \dot{K}_{tip}(t) + \beta_1 \dot{K}_{tip}(t)K_{tip}(t) \tag{8}$$

where β and β_1 are constants given by

$$\beta = \frac{8A_f \eta d l_b}{\pi \delta h E_*}\left(1 + \frac{h}{\lambda d}\right) \tag{9a}$$

$$\beta_1 = \frac{64\sqrt{2}\eta A_f l_b^{3/2}}{3\delta h E_*^2 \pi^{3/2}}\left(1 + \frac{h}{\lambda d}\right). \tag{9b}$$

Under the condition where the displacement, $u(x)$, is small compared to the grain height, d (as is true for sufficiently small l_b), equations (9a) and (9b) reduce to

$$K_{tip}(t) = K_a(t) - \beta \dot{K}_{tip}(t). \tag{10}$$

2.3. Self-consistent formulation

Instead of seeking a global representation of the effect of the bridging tractions [e.g. $K_b(t)$] from a prescribed displacement distribution, as in equation (7), we seek here a displacement distribution which is self-consistent with the corresponding traction distribution. For the general problem this may be accomplished as outlined below.

The displacements due only to an arbitrary, smooth traction distribution in the wake of a crack are given by

$$u^b(x) = \int_0^a \int_x^a G(\alpha, x)G(\alpha, x')p(x') \, d\alpha \, dx' \quad (11)$$

where G is the appropriate Green's function. For the self-consistent solution, where $p(x)$ is a function of $u(x)$, the following relation must be satisfied:

$$u(x) = u^\infty(x) + u^b(x) \quad (12)$$

where $u^b(x)$ is the contribution to the displacement from the bridging tractions, and $u^\infty(x)$ the traction-free displacement distribution along the flank of the crack. For the self-consistent solution, the grain-boundary phase displacements are divided into elastic- and viscous-based components. The relation between these components is determined by using the equality of the elastic and viscous shear stresses in the grain-boundary phase, as outlined in the Appendix A.

While noting that any appropriate traction-free, geometry specific, form may be used for $u^\infty(x)$, we use here the traction-free distribution for a semi-infinite body in plane strain, given by equation (7). It is clear that because the displacements due to the bridging tractions depend on the total crack-flank opening, a local solution along the flank of the crack is necessary in order to provide a self-consistent solution for any non-trivial problem. The methodology used here provides this local solution by discretizing the crack flank and forming a pointwise solution. Where the solution between points is needed [for integration as in equation (5)], a quadratic interpolation of the solution using the adjacent solution points is used:

$$u(\xi) = \frac{1}{2}\xi(\xi - 1)u_{i-1} + (1 - \xi^2)u_i$$

$$+ \frac{1}{2}\xi(\xi + 1)u_{i+1} \quad (13)$$

where

$$\xi = \frac{2x}{x_{i+1} - x_{i-1}} - \frac{x_{i+1} + x_{i-1}}{x_{i+1} - x_{i-1}} \quad (14)$$

and x_i and u_i are the coordinate and displacement at point i, respectively. Note that for all of the solutions done here the velocity, $\dot{u}(x)$, is approximated linearly in time as

$$\dot{u}(x, t) = \frac{u(x, t) - u(x, t - \delta t)}{\delta t}. \quad (15)$$

The self-consistent solution, for a given timestep, is carried out by forming a pointwise error function, F_i, where

$$F_i = u_i - (u_i^b + u_i^\infty). \quad (16)$$

Minimization of the error at each point was done

iteratively by solving the set of equations (in matrix form):

$$[F] = [J][\delta u] \quad (17)$$

where J is the jacobian ($J_{ij} = \partial F_i/\partial u_j$). The solution of equation (17) yields the correction vector, δu, for the current iteration and the process is continued until the pointwise error [equation (16)] is essentially zero, ensuring that a self-consistent solution has been obtained. The solution may subsequently be continued by incrementing time. In order to ensure that a steady-state solution was obtained, the behavior of the normalized crack-tip loading was monitored over time. Plots of normalized crack-tip loading (e.g. K_{max}/K_m, where K_{max} and K_m are the maximum and mean stress intensity of the loading cycle, respectively) vs the reciprocal of the number of applied loading cycles ($1/N$) were found to show a marked change in shape after the attainment of a steady-state condition, as shown in Fig. 4.
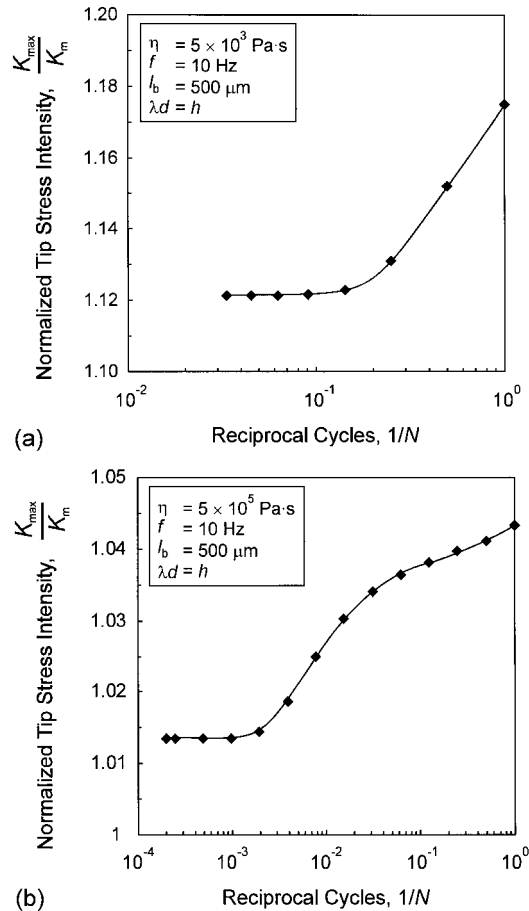

Fig. 4. Plot of the predicted maximum crack-tip stress-intensity, K_{max}, normalized to the mean applied stress intensity, K_m, vs the reciprocal of the cycle number for (a) $\eta = 5 \times 10^3$ Pa s and (b) $\eta = 5 \times 10^5$ Pa s. Steady state is reached when the plot approaches a horizontal line with increasing cycles (time).

2.4. External loading conditions

For both the assumed parabolic crack-opening displacement formulation and the fully self-consistent formulation, solutions were developed under fatigue loading conditions. The applied cyclic waveform, $K_a(t)$, is a sine wave of frequency f, where

$$K_a(t) = K_m + \frac{\Delta K_a}{2} \sin(2\pi f t). \quad (18)$$

Here, $\Delta K_a = K_{max} - K_{min}$ is the amplitude of the applied far-field waveform, where K_{max} and K_{min} are, respectively, the maximum and minimum applied far-field stress intensities, $R = K_{min}/K_{max}$ is the load ratio, and $K_m = \frac{1}{2}(K_{min} + K_{max})$ the stress intensity corresponding to the mean load of the cycle.

3. RESULTS AND DISCUSSION

Solutions were developed under the external loading conditions specified in equation (18), using both the simplified and the fully self-consistent formulations described by equations (10) and (17), respectively. Such solutions allow for a complete description of the crack-opening displacements, $u(x)$, bridging stress distributions, $p(x)$, crack-bridging terms, $K_b(t)$, and crack-tip loading conditions, $K_{tip}(t)$, throughout the loading history. We have used these solutions to explore a wide parameter space in the microstructural and loading variables shown in Table 1 where the range for each variable was chosen to be physically meaningful.

3.1. Parabolic approximation

For the parabolic K_{tip}-controlled approximation with the crack-flank displacements small compared to the grain height $[u(x) \ll d]$, a solution to the simplified differential equation [equation (10)], with applied waveform as given in equation (18), is found to be

$$K_{tip} = K_m + \frac{\Delta K_a}{2} \left\{ \frac{\beta\omega\, e^{-t/\beta}}{1 + \omega^2\beta^2} + \frac{\sin(\omega t - \psi)}{\sqrt{1 + \omega^2\beta^2}} \right\} \quad (19)$$

where $\omega = 2\pi f$, $\psi = \tan^{-1}(\omega\beta)$ and

Table 1. Microstructural and loading parameters investigated in the viscous bridging model

	Range
Loading parameters	
Load ratio, R	$0.1 < R < 0.7$
Frequency, f (Hz)	$0.1 < f < 100$
Load magnitude, ΔK (MPa $\sqrt{m}$)	$1 < \Delta K < 100$
Microstructural parameters	
Viscosity, η (Pa s)	$10^1 < \eta < 10^7$
Area fraction, A_f	1
Grain aspect ratio, d/h	$1 < d/h < 50$
Grain-boundary width, δ (nm)	$0.1 < \delta < 100$
Bridging-zone length, l_b (mm)	$0.25 < l_b < 10$

$$\beta = \frac{8A_f\eta dl_b}{\pi\delta hE}\left(1 + \frac{h}{\lambda d}\right)$$

as previously defined. This solution may serve as a comparison with the self-consistent solutions presented below and provides a rationale for the non-dimensional grouping $\Gamma = \omega\beta$. The form of both the differential equation [equation (10)] and its solution is similar to that solved previously for a single viscous bridging element in the wake of a crack [34]. However, the current model has the advantage of being microstructurally based and, as such, estimates of the loading conditions for a given material may be made as a function of temperature, loading conditions and microstructural variables (e.g. grain morphology and grain boundary composition). Additionally, by ascribing a specific, physically reasonable geometry to the calculations it is possible to evaluate the applicability of the proposed mechanism.

Note that K_{tip} cycles around K_m and is bounded in amplitude by the applied waveform. As might be expected from the viscous model employed here, K_{tip} depends on the applied loading, which is modified by two terms. The first term is a transient, exponentially decaying term with a time constant of β while the other is cyclic and of the same form as the applied loading but is out of phase (lags) by an amount ψ. The cyclic response at the crack tip, ΔK_{tip}, is given by the sum of the two terms, which scale the applied stress-intensity range. For long times ($t \longrightarrow \infty$), the cyclic response at the crack tip is given by the second term which results in the reduction of the applied ΔK given by

$$\frac{\Delta K_{tip}}{\Delta K_a} = \frac{1}{\sqrt{1 + \Gamma^2}} \quad (20)$$

where $\Gamma = \omega\beta$. Figure 5 shows the variation in

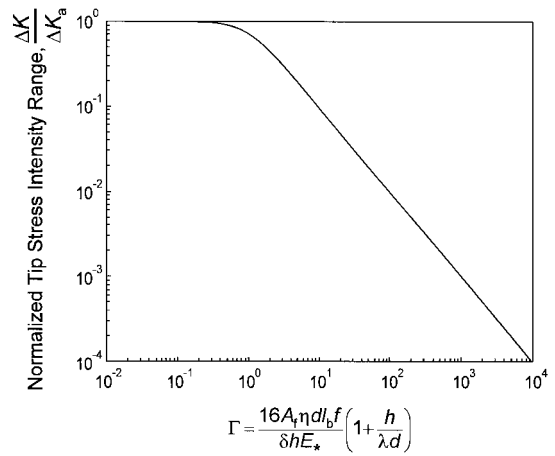$$\Gamma = \frac{16A_f\eta dl_b f}{\delta hE_\star}\left(1 + \frac{h}{\lambda d}\right)$$

Fig. 5. Plot of the predicted crack-tip stress-intensity range, ΔK, normalized to the applied stress intensity range, ΔK_a, vs the non-dimensional parameter Γ for the simplified parabolic approximation. Note that most of the applied loading is damped by $\Gamma \approx 100$.

steady-state normalized crack-tip loading with respect to changes in the non-dimensional grouping, Γ. It is clear that transmission of the applied loading to the crack tip decreases abruptly over the range $1 < \Gamma < 100$, with the normalized cyclic loading, $\Delta K_{tip}/\Delta K_a$, changing from $\sim 70\%$ to less than 1%. For ceramic materials of interest, typical values of loading and microstructural parameters ($E_* = 400$ GPa, $R = 0.1$, $f = 10$ Hz, $d/h = 5$, $\delta = 1$ nm, $l_b = 500\ \mu m$, $h/d \leq \lambda \leq 1$) yield values of Γ between 1 and 10^4 over the range of viscosities, $10^3 < A_f\eta < 10^7$. Note that over this range, the decay constant, β, for the transient term is in the range from ~ 0.1 to 1000 s. In addition, with increasing β, even though the decay time for the transient term becomes increasingly long the magnitudes of both the transient and steady-state terms decrease rapidly. These trends tend to make the system reach steady-state behavior rapidly.

3.2. Self-consistent solution

Results from the self-consistent, visco-elastic solutions are presented in Fig. 6 by showing changes in the normalized crack-tip loading (K_{max}/K_m, K_{min}/K_m) at steady state vs changes in the model parameters. Crack-tip shielding from bridging is seen to grow with increases in grain-aspect ratio, d/h, viscosity, η, and test frequency, f, when the remaining parameters are fixed [Fig. 6(a)–(c), respectively]. Clearly, viscous-film bridging, when active, is an effective shielding mechanism which markedly reduces the stress intensity actually experienced at the crack tip during cyclic fatigue at elevated temperatures. Indeed, recent measurements on silicon nitride in fatigue [42, 43] demonstrate slower growth rates at higher frequency and larger grain size, as our model predicts.

Although there are differences in the assumptions between the parabolic approximation and the self-consistent formulations (Table 2), inspection of the solution for the parabolic K_{tip}-controlled case yields a useful non-dimensional group for characterizing the results of the self-consistent calculations. We again use $\Gamma = \omega\beta$ and, in terms of microstructural and mechanical parameters:

$$\Gamma = \frac{16 A_f \eta d l_b f}{\delta h E_*}\left(1 + \frac{h}{\lambda d}\right). \qquad (21)$$

Variations in the non-dimensional group Γ are explored through changes in the microstructural and loading parameters, as outlined in Table 1.

A comparison of the trends predicted using self-consistent and parabolic solutions is presented in Fig. 7 by plotting the normalized crack-tip cyclic loading, $\Delta K_{tip}/\Delta K_a$, vs the non-dimensional group, Γ. We have indicated which of the model parameters change with changes in Γ as shown by the legend in Fig. 7. It is evident that the parameter, Γ, normalizes the results over the entire range of the
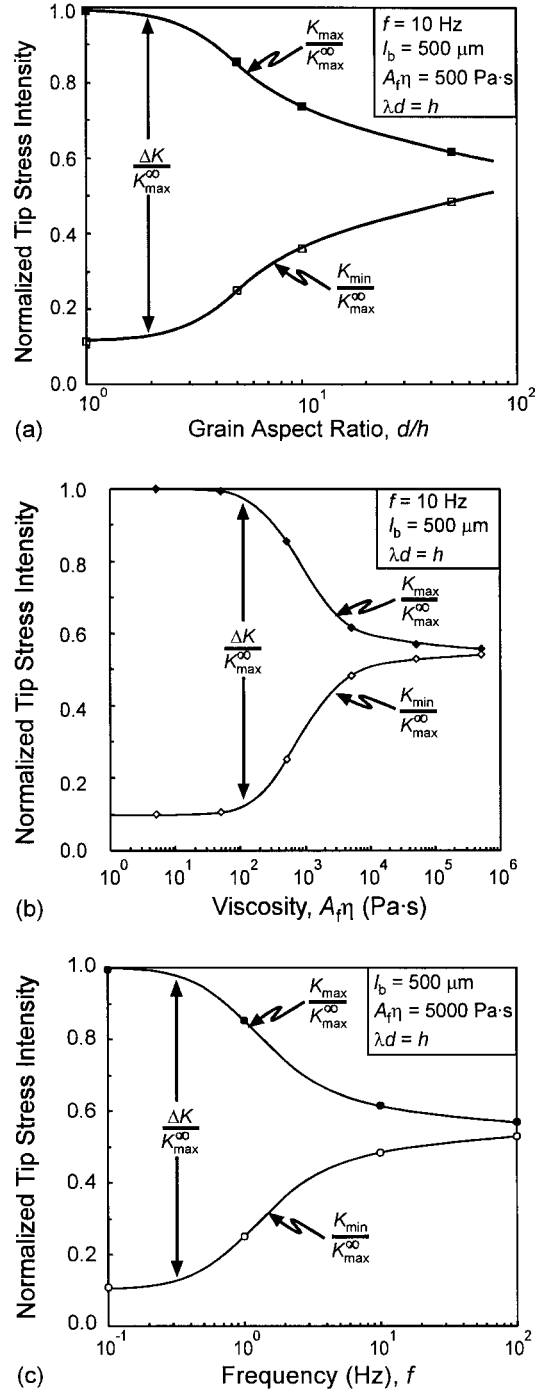

(a)

(b)

(c)

Fig. 6. Self-consistent solution results showing predicted variations in the maximum, K_{max}, and minimum, K_{min}, crack-tip stress intensity, normalized to the maximum applied stress intensity, K_{max}^∞, vs changes in the model parameters, namely (a) grain aspect ratio, d/h, (b) viscosity, η, and (c) frequency, f. The normalized crack-tip stress intensity range, $\Delta K/K_{max}^\infty$, is shown as the difference between the two curves.

parameters studied in the self-consistent formulation here and acts as an appropriate non-dimensional grouping even in this case. Examination of

Table 2. Differences in parabolic and self-consistent formulations

	Parabolic approximation	Self-consistent formulation
Bridging element	Viscous	Viscoelastic
Displacement distribution	Parabolic	Any smooth
Displacement magnitude	$u(x) \ll d$	Any $u(x)$

equation (21) implies that an order of magnitude trade-off exists between the various parameters of the model. For example, an increase in the viscosity by a factor of ten would have exactly the same effect as a decrease in the frequency by a factor of ten.

The variation in the maximum and minimum crack-tip loading, normalized to the mean applied loading ($K_{\max}/K_m$, $K_{\min}/K_m$), shown in Fig. 8, demonstrates that, as expected, the mean applied load is approached asymptotically, with increasing Γ. This is anticipated from the physical form of the bridging traction law [equation (4)] and the results of the parabolic solution. Note that this model predicts that fatigue threshold drops with increasing Γ, as seen in silicon nitride [10], and that cyclic growth rates will always be lower than static growth rates [10, 19]. In cases where the reverse is observed, other damage mechanisms are presumably operating.

Similar to the parabolic approximation, the normalized cyclic loading rapidly changes over the range $1 < \Gamma < 100$ from full to very low transmission of the applied loading to the crack tip. At low Γ, the self-consistent and parabolic solutions converge as expected. Indeed, the parabolic solution is quite robust throughout the most interesting region, e.g. between $0.1 < \Delta K_{\text{tip}}/\Delta K_a < 1$. While the self-consistent solutions conform to trends observed in earlier studies (e.g. Refs [11, 34]), the rigorous nature of our formulation allows for the parameterization of both mechanical and microstructural variables. Furthermore, it identifies a specific range in parameter space where viscous bridging effects are expected to be significant.

At high Γ, where the bridging tractions are largest, the parabolic and self-consistent solutions begin to diverge with the parabolic solution over-predicting the dampening effect of the bridging zone. In part, this is due to the visco-elastic bridging traction law used in the self-consistent solution vs a viscous law necessary for solution of the parabolic model. An additional contribution to this deviation presumably arises from the enforced choice of a parabolic displacement distribution in the case of the parabolic model vs an arbitrary, self-consistent distribution in the full solution.

The displacement distributions along the crack flank are shown in Fig. 9 within the bridging zone. Note that near the end of the bridging zone the displacements in the self-consistent solutions begin to deviate from the parabolic form. This may be anticipated as the self-consistent solutions must converge to the far-field displacements outside of the bridging zone. This convergence could be expected to cause geometry-dependent changes in the self-consistent solutions whenever the bridging zone is comparable to the K-dominant region for the particular geometry chosen. The calculations per-
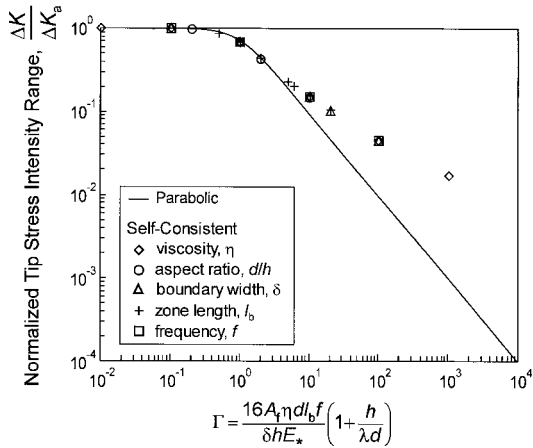

Fig. 7. Self-consistent solution results showing variations in the crack-tip stress-intensity range, ΔK, normalized by the applied stress-intensity range, ΔK_a, vs the non-dimensional parameter Γ. Changes in the individual parameters of the model are shown by symbols while the parabolic solution is denoted by the solid line. Note that the self-consistent solution, which diverges from the parabolic at high Γ, is well represented over the entire range by Γ.
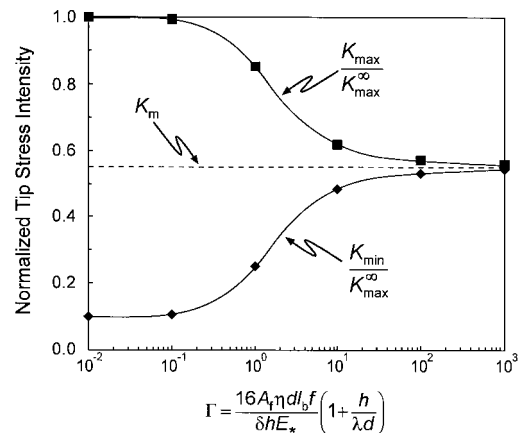

Fig. 8. Self-consistent solution results showing predicted variations in the maximum, $K_{\max}$, and minimum, $K_{\min}$, crack-tip stress intensity, normalized to the maximum applied stress intensity, $K_{\max}^{\infty}$, vs changes in the non-dimensional parameter Γ, showing that the crack-tip loading approaches the mean applied load (dashed line) with increasing Γ.
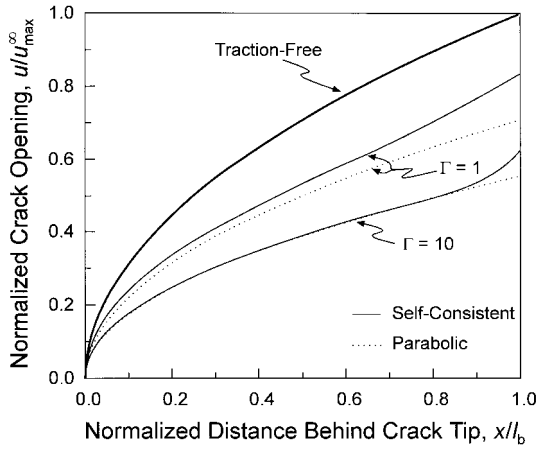
Fig. 9. Crack-opening displacements for parabolic (dashed lines) and self-consistent (solid lines) solutions vs distance behind the crack tip, x, normalized by the bridging zone length, l_b. Displacements, u, are normalized by the maximum traction-free displacement, u_{max}^∞, at the end of the bridging zone.

formed here have implicitly assumed an infinite K-dominant region through the selection of the far-field displacement distribution along the crack flank [equation (7)].

Previous studies (e.g. Refs [25, 31]) indicate that the amount of intergranular glassy phase has a strong effect on high-temperature mechanical properties, with additional glass increasing both creep and fatigue-crack growth rates. The explicit dependence of the current solution may be seen by rearranging equation (21) when $\delta \ll d$, λd, h, as

$$\Gamma = \frac{16A_f \eta l_b f}{V_f h E_*}\left(1 + \frac{h}{\lambda d}\right)\left(1 + \frac{d}{h} + 1/\lambda\right) \quad (22)$$

where V_f is the volume fraction of glassy phase. Hence, an increase in V_f results in a decrease in viscous shielding; where these rate-dependent bridging mechanisms are operative, this presumably leads to faster crack-growth rates.

Due to the sensitivity of the solutions to Γ, changes in test frequency and temperature (because of its large effect on viscosity) would appear to be the most likely of the model variables affecting the crack-tip loading conditions in testing or service. While considerations relating to applied loading frequency can be anticipated directly from the solutions presented here, those involving viscosity are more difficult to quantify. This is due to the scarcity of information relating to the composition and structure of the grain-boundary phase and the relative absence of viscosity data on such boundaries. In order to investigate the anticipated response of a material under test or service conditions, over a given temperature range, we use a model material with values of elastic modulus, E_*, grain boundary thickness, δ, grain size, d/h, and bridging-zone length, l_b, given in Table 3.

Table 3. Parameter values for model system

Parameter	Value
R	0.1
f	10 Hz
E_*	400 GPa
A_f	0.1
d/h	5
δ	1 nm
l_b	500 μm
λ	h/d (rod-like grains)

The temperature dependence of the loading conditions enters through the viscosity, which is assumed to follow the familiar form:

$$\eta = \eta_0\, e^{-Q/RT} \quad (23)$$

where Q is the activation energy for viscous flow, η_0 is a scaling parameter, and R here is the gas constant. Two Si_3N_4-based systems are considered, one very high purity [44], the other, an older, lower-purity commercial grade [45]. A plot of the normalized cyclic crack-tip loading, $\Delta K_{tip}/\Delta K_a$, vs temperature is presented in Fig. 10 where, for the higher purity Si_3N_4, the temperature range has been limited to below onset of material decomposition [46]. This plot demonstrates how rapidly the loading conditions can change with a change in the test conditions for the lower purity Si_3N_4. Additionally, it is clear that for the higher purity Si_3N_4, tested in an inert environment, a viscous boundary phase would be unlikely to affect test conditions. The stark differences in the temperature ranges over which viscous bridging may affect crack-tip loading conditions underscores the importance of the prop-
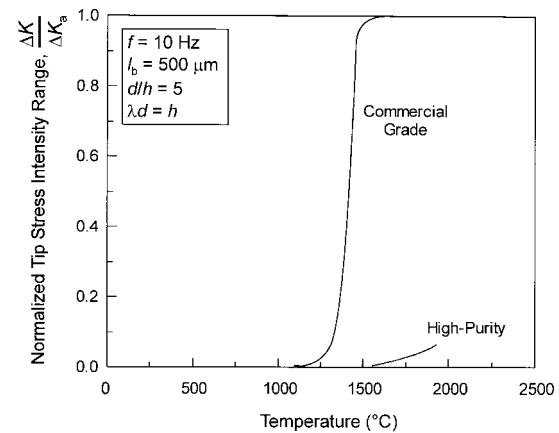

Fig. 10. Predicted variation in the crack-tip stress-intensity range, ΔK, normalized by the applied stress-intensity range, ΔK_a, vs temperature for two Si_3N_4 materials. Material A [45] is a presumably low-purity commercial material while material B [44] has been fabricated to minimize impurity content. The crack-tip stress-intensity range is predicted to have a strong temperature dependence for the lower-purity material while the grain boundary in the high-purity material is expected to show no viscous effects up to the disassociation of the Si_3N_4.

erties of the grain-boundary films in affecting the overall mechanical behavior of the material.

4. SUMMARY AND CONCLUSIONS

A model for grain bridging during cyclic fatigue-crack growth in ceramics at elevated temperatures has been proposed which includes both the applied loading conditions and the microstructure. The model seeks to investigate the driving force at the crack tip over a wide range of microstructural parameters and applied loading conditions. The fundamental bridging unit is composed of a rigid grain whose movement is resisted by a visco-elastic grain-boundary film. Through this unit such variables as grain size and shape, grain-boundary thickness and viscosity, and bridging-zone length are introduced.

Both a simplified parabolic and completely self-consistent solution have been obtained for the case of an applied cyclic load. For the simplified parabolic approximation, a closed-form solution is possible while in the self-consistent case numerical methods were used to find a solution over a wide, physically plausible range of the model parameters. The parabolic solution provides a rational for the appropriate non-dimensional grouping and this group, $\Gamma = 16A_f\eta dl_b f(1 + h/\lambda d)/\delta hE_*$, is found to describe the response even in the case of the self-consistent solution. At small Γ, where the bridging zone is relatively weak, the solutions converge as expected. However, the parabolic solution is found to be surprising robust at describing the amount of crack-tip shielding over most of the parameter space.

As expected from the viscous nature of the bridging element, increases in the magnitude of the response of the bridging tractions (increasing Γ) lead to a reduction in the transmittance of the cyclic loading from the far-field to the crack tip, which approaches a constant driving force equal to the mean applied load.

Application of the model to two Si_3N_4 systems, one high purity and one commercial grade, has identified that the *local* crack-tip loading conditions, through the viscosity, are expected to have a strong temperature dependence. For the higher purity system, where the viscosity of the grain-boundary phase is relatively high throughout the stable thermodynamic range, the viscous grain-bridging mechanism would not be expected to play a role. However, as the viscosity of the boundary phase is expected to depend strongly on impurity content, contamination of the material during test or service conditions may result in activation of this type of mechanism. This last point should be emphasized since the viscous behavior of the grain-boundary film may change over time due to both anticipated thermodynamic evolution of the as-processed material as well as by impurity addition from environmental sources.

REFERENCES

1. Rahaman, M. N., *Ceramic Processing and Sintering*. Marcel Dekker, New York, 1995.
2. Tsai, R. L. and Raj, R., *Acta metall.*, 1982, **30**, 1043.
3. Chen, I.-W., Liu, S.-Y. and Jacobs, D., *Acta metall. mater.*, 1995, **34**, 1439.
4. Thouless, M. D., *J. Am. Ceram. Soc.*, 1988, **71**, 408.
5. Rouxel, T. and Wakai, F., *Acta metall. mater.*, 1993, **41**, 3203.
6. Evans, A. G. and Rana, A., *Acta metall.*, 1980, **28**, 129.
7. Wilkinson, D. S. and Vitek, V., *Acta metall.*, 1982, **30**, 1723.
8. Evans, A. G. and Wiederhorn, S. M., *J. Mater. Sci.*, 1974, **9**, 270.
9. Knickerbocker, S. H., Zangvil, A. and Brown, S. D., *J. Am. Ceram. Soc.*, 1985, **68**, C99.
10. Ramamurty, U., Hansson, T. and Suresh, S., *J. Am. Ceram. Soc.*, 1994, **7**, 2985.
11. Dey, N., Socie, D. F. and Hsia, K. J., *Acta metall. mater.*, 1995, **43**, 2163.
12. Jenkins, M. G., Ferber, M. K. and Lin, C.-K. J., *J. Am. Ceram. Soc.*, 1993, **76**, 788.
13. Kossowsky, R., *J. Am. Ceram. Soc.*, 1973, **56**, 531.
14. Horibe, S. and Sumita, M., *J. Mater. Sci.*, 1988, **23**, 3305.
15. Holmes, J. W., *J. Am. Ceram. Soc.*, 1991, **74**, 1639.
16. Fett, T., Himsolt, G. and Munz, D., *Adv. Ceram. Mater.*, 1986, **1**, 179.
17. Lin, C.-K. J. and Socie, D. F., *J. Am. Ceram. Soc.*, 1991, **74**, 1511.
18. Lin, C.-K. J., Socie, D. F., Xu, Y. and Zangvil, A., *J. Am. Ceram. Soc.*, 1992, **75**, 637.
19. Huang, C.-H. and Shang, J. K., *Acta metall. mater.*, 1995, **43**, 4179.
20. Yao, D. and Shang, J. K., *Acta metall. mater.*, 1994, **42**, 589.
21. Yao, D. and Shang, J. K., *J. Am. Ceram. Soc.*, 1994, **77**, 2911.
22. Liu, S.-Y., Chen, I.-W. and Tien, T.-Y., *J. Am. Ceram. Soc.*, 1994, **77**, 137.
23. Liu, S.-Y. and Chen, I.-W., *Acta mater.*, 1996, **44**, 2079.
24. Han, L. X. and Suresh, S., *J. Am. Ceram. Soc.*, 1989, **72**, 1233.
25. Ewart, L. and Suresh, S., *J. Mater. Sci.*, 1992, **27**, 5181.
26. Haubensak, F. G. and Dauskardt, R. H., Presentation at the 47th Pacific Coast Regional Meeting of the American Ceramic Society, Seattle, November 1995.
27. Ueno, A., Kishimoto, H. and Kawamoto, H., in *Fracture Mechanics of Ceramics*, Vol. 9, ed. R. C. Bradt *et al.* Plenum Press, New York, 1992, p. 423.
28. Kishimoto, H., Ueno, A., Kawamoto, H. and Tomitaka, A., *J. Soc. Mater. Sci. Japan*, 1992, **41**, 1805 (in Japanese).
29. Ueno, A., Kishimoto, H., Kawamoto, H. and Murasawa, T., *J. Soc. Mater. Sci. Japan*, 1993, **42**, 976 (in Japanese).
30. Evans, A. G., Russell, L. R. and Richerson, D. W., *Metall. Trans.*, 1975, **6A**, 707.
31. Zhang, Y. H. and Edwards, L., *Mater. Sci. Engng*, 1998, **A256**, 144.
32. Gilbert, C. J., Dauskardt, R. H. and Ritchie, R. O., *J. Am. Ceram. Soc.*, 1995, **78**, 2291.
33. Gilbert, C. J. and Ritchie, R. O., *Acta mater.*, 1998, **46**, 609.
34. Ramamurty, U., *J. Am. Ceram. Soc.*, 1996, **79**, 945.

35. Evans, A. G. and Fuller, E. R., *Metall. Trans.*, 1974, **5**, 27.
36. Lathabai, S., Rödel, J. and Lawn, B. R., *J. Am. Ceram. Soc.*, 1991, **74**, 1360.
37. Dauskardt, R. H., *Acta metall. mater.*, 1993, **41**, 2765.
38. Yi, K. S., Cox, B. N. and Dauskardt, R. H., *J. Mech. Phys. Solids*, submitted.
39. Geiger, G. H. and Poirier, D. R., *Transport Phenomena in Metallurgy*. Addison-Wesley, Reading, MA, 1973.
40. Lawn, B. R., *Fracture of Brittle Solids*, 2nd edn. Cambridge University Press, New York, 1993.
41. Irwin, G. R., *Hanbuch der Physik*, Vol. 6. Springer-Verlag, Berlin, 1958, p. 551.
42. Miyashita, Y., Maruta, H., Mutoh, Y., Zhu, S. and Hansson, T., in *Proc. Sixth International Symposium on Ceramic Materials and Components for Engines*, Arita, Japan, ed. K. Niihara, S. Kanzaki, K. Komeya, S. Hirano and K. Morinaga. Technoplaza Co. Ltd, Tokyo, Japan, 1998.
43. Hansson, T., Miyashita, Y. and Mutoh, Y., in *Fracture Mechanics of Ceramics*, Vol. 12, ed. R. C. Bradt *et al.* Olenum Press, New York, 1996, p. 187.
44. Pezzotti, G., Ota, K. and Kleebe, H.-J., *J. Am. Ceram. Soc.*, 1996, **9**, 2237.
45. Mosher, D. R., Raj, R. and Kossowsky, R., *J. Mater. Sci.*, 1976, **11**, 49.
46. Pehlke, R. D. and Elliott, J. F., *Trans. metall. Soc. A.I.M.E.*, 1959, **215**, 781.

APPENDIX A

Separation of elastic- and viscous-based displacements

For the viscoelastic boundary phase with geometry defined in Fig. 3 and described by a simple Maxwell model, the displacements may be partitioned as

$$u = u_e + u_\eta \qquad (A1)$$

where u_e and u_η are the elastic and viscous portions of the total displacement, u. The elastic and viscous shear stresses in the fluid are given by

$$\tau_e = \frac{2Gu_e}{\delta} \qquad (A2)$$

$$\tau_\eta = \frac{2\eta}{\delta}\frac{du_\eta}{dt} \qquad (A3)$$

where G is the shear modulus of the viscoelastic boundary phase, η the viscosity, and du_η/dt the relative velocity of the adjacent grains. A linear velocity gradient across the fluid, of width δ, is assumed. By equating the elastic and viscous shear stresses, the relation between the elastic and viscous displacements is obtained as

$$u_\eta = \frac{u}{1 + \dfrac{\eta}{G}\dfrac{du_\eta}{dt}}. \qquad (A4)$$